

---

# Uncovering the Topology of Time-Varying fMRI Data using Cubical Persistence

---

Bastian Rieck<sup>\*,†</sup>    Tristan Yates<sup>\*,‡</sup>    Christian Bock<sup>†</sup>    Karsten Borgwardt<sup>†</sup>  
 Guy Wolf<sup>§,¶</sup>    Nicholas Turk-Browne<sup>‡,||</sup>    Smita Krishnaswamy<sup>‡,||</sup>

## Abstract

Functional magnetic resonance imaging (fMRI) is a crucial technology for gaining insights into cognitive processes in humans. Data amassed from fMRI measurements result in volumetric data sets that vary over time. However, analysing such data presents a challenge due to the large degree of noise and person-to-person variation in how information is represented in the brain. To address this challenge, we present a novel topological approach that encodes each time point in an fMRI data set as a persistence diagram of topological features, i.e. high-dimensional voids present in the data. This representation naturally does not rely on voxel-by-voxel correspondence and is robust towards noise. We show that these time-varying persistence diagrams can be clustered to find meaningful groupings between participants, and that they are also useful in studying within-subject brain state trajectories of subjects performing a particular task. Here, we apply both clustering and trajectory analysis techniques to a group of participants watching the movie ‘Partly Cloudy’. We observe significant differences in both brain state trajectories and overall topological activity between adults and children watching the same movie.

## 1 Introduction

Human cognitive processes are commonly studied using functional magnetic resonance imaging (fMRI), amassing highly complex, well-structured, and time-varying data sets across multiple individual subjects. fMRI uses blood oxygen measurements of 3D brain volumes divided into voxels (3D pixels with dimensions in the mm range). Voxels are measured over time while participants perform cognitive tasks, resulting in time-varying activity measurements and an activation function over the volume. The ultimate goal of extracting higher-level abstractions from such data is primarily impeded by two factors: (i) the measurements are inherently noisy, due to changes in machine calibration, spurious patient movements, and environmental conditions, (ii) there is a high degree of variability even between otherwise healthy brains (e.g. in terms of the representation of stimulus and activity in the brain). While these factors can be mitigated by certain experimental protocols and pre-processing decisions, they cannot be fully eliminated. This demonstrates the need for using representations that are to some extent *robust* with respect to noise and *invariant* with respect to isometric transformations in order to better capture cognitively-relevant fMRI activity, particularly across populations where anatomy–function relations may differ.

---

\*These authors contributed equally.

||These authors jointly supervised this work.

†Department of Biosystems Science and Engineering, ETH Zurich, Switzerland

‡Department of Psychology, Yale University, New Haven, CT, USA

§Department of Mathematics & Statistics, Université de Montréal, Montréal, QC, Canada

¶Mila – Quebec AI Institute, Montréal, QC, Canada

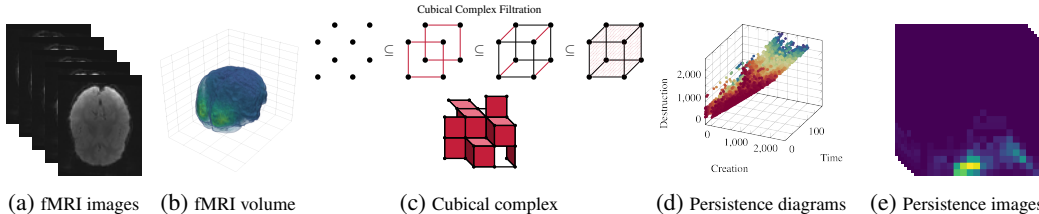


Figure 1: A graphical overview of our method. We represent an fMRI stack (a) as a volume (b), from which we create a sequence of cubical complexes (c). Calculating the persistent homology of this sequence results in a set of time-varying persistence diagrams (d); note that we only show the diagrams for a single dimension of the cubical complex. We calculate summary statistics from the diagrams (not shown), and convert them to vectorial representations (e) for analysis tasks.

Traditional approaches largely ignore these factors, considering them inevitable noise in the measurements. Voxel activity is often either directly compared across different cognitive tasks, or the time-varying activity of voxels in pre-defined brain regions sharing functional properties is correlated to create a ‘functional connectivity’ graph. Our approach differs from existing approaches for fMRI data analysis in two crucial ways, namely (i) it is coordinate-free, providing a stable representation of high-level brain activity, even without a voxel-by-voxel match, and (ii) it does *not* require the creation of a correlation graph, or operate on any other approximated graph structure (in contrast to the MAPPER algorithm [48], for example). Instead, our method uses the ‘raw’ voxel activations themselves as a cubical complex, which we further characterise using time-varying persistence diagrams that indicate the presences of topological features such as voids of various dimensions in the voxel activations. These topological features are naturally invariant to a variety of shifts and noise (see Section 4). Our formulation enables the non-parametric analysis of fMRI data both statically and dynamically, i.e. for assessing differences between cohorts across time, and enabling insights into time-varying topological brain state trajectories within cohorts or individuals. For individuals, we use an averaged summary statistic over time that can be embedded to explore population structure and variability statically, which we use to organise subjects in our test set by age. Then, after clustering subjects into cohorts, we propose a novel method for producing a time-varying trajectory of persistence diagrams that can be used to quantify the progression and entropy of brain states. In summary, we make the following contributions:

- We present a novel non-parametric framework for transforming time-varying fMRI data into time-varying topological representations.
- We empirically show that these representations (a) capture age-related differences, and (b) shed light on the cognitive processes of age-stratified cohorts.
- Finally, we show that our topological features are more informative for an age prediction task than other representations of the data set.

## 2 Background on topological data analysis

Topological data analysis (TDA) recently started gaining traction in machine learning [11, 25–28, 30, 33, 38, 40, 41, 43, 59]. TDA is a rapidly-growing field that provides tools for analysing the shape of data sets. This section provides a brief overview, aiming primarily for intuition and less for depth (see also Section A.1 for a worked example). We refer to Edelsbrunner and Harer [20] for details. To our knowledge, this is the first time that TDA has been *directly* applied to fMRI data (as opposed to applying it on auxiliary representations such as functional connectivity networks).

**Simplicial homology.** The central object in algebraic topology is a simplicial complex  $K$ , i.e. a high-dimensional generalisation of a graph, containing simplices of varying dimensions: vertices, edges, triangles, tetrahedra, and their higher-dimensional counterparts. A graph, for example, can be seen as a 1-dimensional simplicial complex, containing vertices and edges. Such complexes are primarily used to describe topological objects such as manifolds<sup>1</sup>. Simplicial homology refers to a

<sup>1</sup>We deviate from this notion in this paper but follow the conventional exposition, which focuses primarily on a simplicial view.

framework for analysing the connectivity of  $K$  via matrix reduction algorithms, assigning  $K$  a graded set of mathematical groups, the homology groups. Homology groups describe the topological features of  $K$ ; in low dimensions  $d$ , these features are called *connected components* ( $d = 0$ ), *tunnels* ( $d = 1$ ), and *voids* ( $d = 2$ ), respectively. The number of  $d$ -dimensional topological features is referred to as the  $d$ th Betti number  $\beta_d \in \mathbb{N}$ ; it is used to distinguish between different topological objects: for example, a circle (i.e. the *boundary* of a disk) has Betti numbers  $(1, 1)$  because there is a single connected component and a single tunnel, while a filled square has Betti numbers  $(1, 0)$ .

**Persistent homology.** The analysis of real-world data sets, having no preferred scale at which features occur, requires a different approach: Betti numbers cannot be directly used here because they only represent counts, i.e. a single scale. Endowing them with additional information leads to *persistent homology*, an extension of simplicial homology that requires a simplicial complex  $K$  and an additional function  $f: K \rightarrow \mathbb{R}$ , such as an activation function. If  $f$  only attains a finite set of function values  $f_0 \leq f_1 \leq \dots \leq \dots \leq f_{m-1} \leq f_m$ , one can sort  $K$  according to them, leading to a *filtration*—a nested sequence of simplicial complexes

$$\emptyset = K_0 \subseteq K_1 \subseteq \dots \subseteq K_{m-1} \subseteq K_m = K, \quad (1)$$

with  $K_i := \{\sigma \in K \mid f(\sigma) \leq f_i\}$ . Filtrations represent the evolution of  $K$  along  $f$ . Similar to the Watershed transform in image processing [42], topological features can be *created* (a new connected component might arise) or *destroyed* (two connected components might merge into one) in a filtration. Persistent homology efficiently tracks topological features across a filtration, representing each one of them as a tuple  $(f_i, f_j) \in \mathbb{R}^2$ , with  $i \leq j$  and  $f_i, f_j \in \text{im}(f)$ .

**Persistence diagrams.** The tuples  $(f_i, f_j)$  are collected according to their dimension  $d$  and stored in the  $d$ th *persistence diagram*  $\mathcal{D}_d$ , which summarises all  $d$ -dimensional topological activity. As a consequence of the calculation process, all points in  $\mathcal{D}_d$  are situated *above* the diagonal. The quantity  $\text{pers}(x, y) := |y - x|$ , i.e. the distance to the diagonal (up to a constant factor), of a point  $(x, y) \in \mathcal{D}_d$  is called the *persistence* of its corresponding topological feature. Low-persistence features used to be considered ‘noise’, while high-persistence features are assumed to correspond to ‘real’ features of a data set [21]. Recent work cast some doubts as to whether this assumption is justified [9]; in medical data, low persistence merely implies ‘low reliability’, *not* necessarily ‘low importance’.

### 3 Related work

For fMRI analysis, the typical approach is to compare voxel activations directly, but when one is interested in time-varying activity from a continuous stimulus (e.g. while watching a movie or resting), voxel data is sometimes transformed into correlation matrices, either calculated across *time points* [4] or across *voxels* [57] (studying functional connectivity, i.e. information about the connectivity between brain regions sharing certain functional properties). Due to the size of the matrices in the latter case, one also often reduces the dimensionality by applying an atlas parcellation [47]. Both of these representations are efficacious, with voxel-by-voxel correlation matrices providing insights into the topology and dynamics of human brain networks [52]. Moreover, for many multi-subject fMRI studies, *shared response models* [13], abbreviated as SRMs, have proven effective. SRMs ‘learn’ a mapping of multiple subjects into the same space, enabling the detection of group differences, or the study of relations between brain activity and movie annotations, for example [54]. Recently, SRM was used to map voxel activity into a functional space (as opposed to an anatomical one), to study the brain representation of, among others, visual and auditory information while receiving naturalistic audiovisual stimuli [29]. Nonetheless, while SRM is one of the most powerful techniques for extracting cognitively-relevant signals from fMRI data, there is still room for improvement.

Previous work fusing fMRI analysis and topological data analysis is either based on auxiliary (topological) representations [44, 49], such as the MAPPER algorithm [48] which operates on graphs, and requires numerous parameter choices, or it makes use of functional connectivity information (information about connectivity between brain regions sharing functional properties) and pre-defined regions of interest [3, 22, 24, 45]. By contrast, our method operates *directly* on fMRI volumes, requiring neither additional location information nor auxiliary representations. We will instead make use of *cubical complexes*, for which we essentially replace triangles by squares and tetrahedra by cubes (see Figure 1c and the subsequent section for details). Cubical complexes and their homology are well-studied in algebraic topology, but their use in real-world applications used to be limited to

image segmentation [2]. This changed with the rise of persistent homology, which was extended to the cubical setting [37, 51, 55], leading to cubical persistent homology [18, 34, 56].

## 4 A topology-based framework for fMRI data sets

In the following, we will be dealing with time-varying fMRI. By this, we mean that we are observing an activation function  $f: \mathcal{V} \times \mathcal{T} \rightarrow \mathbb{R}$  over a 3D bounded volume  $\mathcal{V} \subset \mathbb{R}^3$  and a set of time steps  $\mathcal{T}$ . The alignment of  $\mathcal{V}$  across different subjects is highly non-trivial; we provide more details about this at the beginning of Section 5. For  $t \in \mathcal{T}$ , the function  $f(\cdot, t)$  is typically visualised using either stacks of images (Figure 1a) or volume rendering (Figure 1b). While it would be possible to analyse the topology of individual images [7], we want a holistic view of the topology of  $\mathcal{V}$ . To this end, we transform  $\mathcal{V}$  into a *cubical complex*  $C$ , i.e. an equivalent of a simplicial complex, in which triangles and tetrahedra are replaced by squares and cubes (see Figure 1c). Cubical complexes are perfectly suited to represent an fMRI volume  $\mathcal{V}$  because each voxel corresponds precisely to one cubical simplex (whereas if we were to use a simplicial complex, we would have to employ interpolation schemes as there is no natural mapping from voxels to tetrahedra; see Figure A.3 for more details).

**Terminology.** We assume that we are given a data set of  $n$  volumes  $\mathcal{V}_1, \dots, \mathcal{V}_n$ , corresponding to  $n$  different individuals, and a set of  $m$  time steps  $\mathcal{T} = \{t_1, \dots, t_m\} \subset \mathbb{N}$ . We use  $\text{vert}(\mathcal{V}_i)$  to denote the vertex (i.e. voxel) set of  $\mathcal{V}_i$ , and  $f_i$  to denote its activation function, i.e.  $f_i: \mathcal{V}_i \times \mathcal{T} \rightarrow \mathbb{R}$ . Here, the activation functions are *aligned* with respect to their time steps; this is an assumption that greatly simplifies all subsequent analysis steps. It does not impose a large restriction in practice.

**Topological features from fMRI data.** We obtain topological features of each  $f_i$  following a three-step procedure, namely (1) cubical complex conversion, (2) filtration calculation, and (3) persistence diagram calculation. The *conversion* of a volume  $\mathcal{V}_i$  to a cubical complex  $C_i$  is simple, as  $\mathcal{V}_i$  and  $C_i$  share the same cubical elements and connectivities. Thus, the vertices of  $C_i$  are the voxels of  $\mathcal{V}_i$  and there are edges between neighbouring vertices as defined by a regular 3D grid, in which each vertex has six neighbours (two per coordinate axis). These neighbourhoods implicitly define the connectivity of higher-dimensional elements (squares and cubes). We will use  $\sigma$  to denote an element of a cubical complex<sup>2</sup>. Next, we impose a *filtration*—an ordering—of the elements of  $C_i$ . Since we want to analyse topological features over time, we have to calculate a filtration for every time step. Given  $t_j \in \mathcal{T}$ , we assign the values of  $f_i(\cdot, t_j)$  to  $C_i$ . We use the most natural assignment: each vertex (voxel) of  $C_i$  receives its activation value at time  $t_j$ , while a higher-dimensional element  $\sigma$  is assigned a value recursively via  $f_i(\sigma, t_j) := \max_{v \in \text{vert}(\sigma)} f_i(v, t_j)$ . We then sort the cubical complex  $C_i$  in ascending order according to these values; in case of a tie, a lower-dimensional element (e.g. an edge) precedes a higher-dimensional one (e.g. a square). Having obtained a filtration according to Equation 1, we may now calculate the persistent homology of  $C_i$  at time step  $t_j$ , resulting in a collection of *persistence diagrams*. Since each  $\mathcal{V}_i$  is three-dimensional, we obtain a triple  $(\mathcal{D}_0^{(i,j)}, \mathcal{D}_1^{(i,j)}, \mathcal{D}_2^{(i,j)})$  for every time step  $t_j$ ; persistence diagrams for  $d \geq 3$  are all empty. Notice that the calculation of persistence diagrams for a participant  $i$  and a time step  $t_j$  can be easily parallelised, since we treat time steps independently. Subsequently, we will use  $\mathcal{D}^{(i)}$  to denote the set of all persistence diagrams associated with the  $i$ th participant. We can plot the resulting persistence diagrams of each participant as a set of diagrams in  $\mathbb{R}^3$ , with the additional axis being used to represent *time* (Figure 1d).

The filtration that we employ here is also known as a *sublevel set filtration*. Other filtrations could also be used (our method is not restricted to any specific one), but a symmetry theorem [16] states that, unless we are willing to modify the activation function values themselves, we are not gaining any more information about the topology of our input data. For the subsequent analyses, we will be dealing with collections of persistence diagrams  $\mathcal{D}^{(i)}$ . The space of persistence diagrams affords several metrics [15, 17], but they are computationally expensive and infeasible for the cardinalities we are dealing with (a typical persistence diagram of a participant contains about 10000 features). We will thus be working with *topological summary statistics* and *persistence diagram vectorisations*.

<sup>2</sup>These elements are the ‘simplices’ of the cubical complex, but we refrain from re-using the term ‘simplex’ so as not to confuse ourselves or the reader.

**Properties.** Prior to delving deeper into our pipeline, we describe some properties of our approach and why topological features are advantageous. Topology is inherently coordinate-free, meaning that all the features we describe are invariant to homeomorphism, i.e. stretching and bending. Moreover, the persistence diagrams of spaces of different cardinalities and scales can be compared, making it possible to ‘mix’ participants from studies with different imaging modalities or resolutions (of course, this should not be done indiscriminately). Arguably the largest advantage of persistent homology is its stability with respect to perturbations. This is quantified by the following theorem, whose proof we defer to [Section A.6](#).

**Theorem 1.** *Let  $f: \mathcal{V} \rightarrow \mathbb{R}$  and  $g: \mathcal{V} \rightarrow \mathbb{R}$  be two activation functions. Then their corresponding persistence diagrams  $\mathcal{D}_f$  and  $\mathcal{D}_g$  satisfy  $W_\infty(\mathcal{D}_f, \mathcal{D}_g) \leq \|f - g\|_\infty$ , where  $W_\infty$  denotes the bottleneck distance between persistence diagrams [15], defined as  $W_\infty(\mathcal{D}_f, \mathcal{D}_g) := \inf_{\eta: \mathcal{D} \rightarrow \mathcal{D}_g} \sup_{x \in \mathcal{D}_f} \|x - \eta(x)\|_\infty$ , with  $\eta: \mathcal{D}_f \rightarrow \mathcal{D}_g$  denoting a bijection between the points of the two diagrams, and  $\|\cdot\|_\infty$  referring to the  $L_\infty$  norm.*

The consequence of this stability theorem is that the persistence diagrams that we calculate are stable with respect to perturbations, provided those perturbations are of small amplitudes. This is a desirable characteristic for a feature descriptor because it provides us with well-defined bounds for its behaviour under noise. A more precise version of this stability theorem exists [17], but requires a more involved setup<sup>3</sup>, which we leave for future work. In general, we note that time-varying TDA is still a rather nascent sub-field of TDA. A standard approach, namely the calculation of ‘persistence vineyards’ [14], resulting in a decomposition of a time-varying persistence diagram into individual ‘vines’, is not applicable here because the changes between different time steps are not infinitesimal (there *is* a large amount of temporal coherence between consecutive time steps, but there is no guarantee that the change between them is upper-bounded). It is still unknown in our setting whether a vineyard representation with unique vines exists at all [35]. We therefore prefer to treat the individual time steps as independent calculations but note that future work should address a more efficient computation by exploiting similarities between consecutive time steps.

**Implementation and complexity.** While the general calculation of persistent homology on high-dimensional simplicial complexes is still computationally expensive, there are highly-efficient algorithms for lower-dimensional calculations [6]. Here, we use DIPHA [5], a distributed implementation of persistent homology, as it implements an efficient algorithm for computing topological features of cubical complexes [55]. Space and time complexity is linear in the number of voxels, so our conversion process does not change the complexity of processing the data. The persistent homology calculation has a time complexity of  $\mathcal{O}(|\mathcal{V}|^\omega)$ , with  $\omega \approx 2.376$  [31]. The distributed implementation of DIPHA is reported [5] to be capable of calculating persistent homology for  $|\mathcal{V}| \approx 10^9$ , making our pipeline feasible and scalable. For the persistence image calculation in [Section 5.2](#), we use Scikit-TDA [46]. We make our code available to ensure reproducibility.

## 5 Results

We evaluate our topological pipeline using open-source fMRI data [39], available on the OpenNeuro database (accession number ds000228). The participants comprised 33 adults (18–39 years old;  $M = 24.8$ ,  $SD = 5.3$ ; 20 female) and 122 children (3.5–12 years old;  $M = 6.7$ ,  $SD = 2.3$ ; 64 female) who watched the same animated movie ‘Partly Cloudy’ [50] while undergoing fMRI. Please refer to [Section A.3](#) and Yates et al. [58] for a full description of the pre-processing. The relevant outputs of these pre-processing steps are: a 4-dimensional ( $x \times y \times z \times t$ , with  $x, y, z$  being coordinates, and  $t$  representing time) fMRI time series and a whole-brain mask (BM) for each individual subject. The fMRI time series includes 168 time steps (each comprising 2 s of the movie) that correspond to the same point in the movie for each subject; since for the first five time steps only a blank screen was shown, we remove these plus two time steps to account for the fMRI hemodynamic lag for all analyses. We supplemented the whole-brain mask by also creating an ‘occipital-temporal’ mask (OM) for each subject. This entailed finding the intersection between an individual subject’s whole-brain mask and occipital, temporal, and precuneus regions of interest defined from the Harvard–Oxford cortical atlas. If our results reflect patterns relevant to cognitive processing, we would expect similar—if not better results—using this occipital-temporal mask, since it contains the regions most consistently involved

<sup>3</sup>We will have to show Lipschitz continuity for the functions, plus certain other properties of the space  $\mathcal{V}$ .

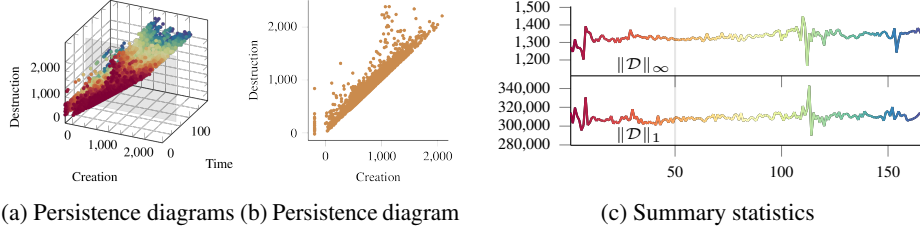


Figure 2: Example of summary statistics calculations. Starting from a sequence of time-varying persistence diagrams (a) of one participant, for each diagram slice (b), we evaluate a scalar-valued statistic  $S: \mathcal{D} \rightarrow \mathbb{R}$ , leading to a time series (c); the corresponding time point is highlighted.

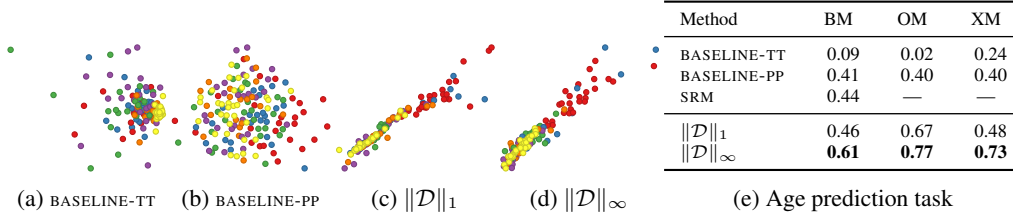


Figure 3: An embedding of the *distances* for different baselines and topological summaries, based on the whole-brain mask (BM); colour-coding refers to the age group of participants. The table depicts the results of the age prediction task, stratified by different brain masks; performance is measured as a correlation coefficient (bold indicates the best results).

in movie-watching (e.g. visual regions). Last, we also calculated the ‘logical XOR’ between the whole-brain mask and the occipital-temporal mask; this mask (XM) makes it possible to study the relevance of topological features with respect to non-visual regions (including the frontal lobe) in the brain. To prevent analysis bias, data were initially fully unlabelled during the development of our pipeline. Later on, participants were assigned to cohorts based on their age group, using the same bins as Yates et al. [58]; we initially did not know whether cohorts were sorted in ascending or descending order. The actual ages were only used in the age prediction experiment, which was performed *after* method development had ceased.

### 5.1 Static analysis based on summary statistics

Extracting information from the time-varying persistence diagrams of each participant is impeded by their complex geometrical structure, making it necessary to use summary statistics. We first focus on a description of *global* properties of participants, restricting ourselves to persistence diagrams with  $d = 2$  (i.e. we are studying voids of the activation function). To this end, we calculate topological summary statistics of the form  $S: \mathcal{D} \rightarrow \mathbb{R}$ . We calculate two related summary statistics here, namely the *infinity norm*  $\|\mathcal{D}\|_\infty$  of a persistence diagram [15] and the *p-norm*<sup>4</sup>  $\|\mathcal{D}\|_p$  [12, 17], defined by

$$\|\mathcal{D}\|_\infty := \max_{x,y \in \mathcal{D}} \text{pers}(x,y)^p \quad \text{and} \quad \|\mathcal{D}\|_p := \sqrt[p]{\sum_{x,y \in \mathcal{D}} \text{pers}(x,y)^p}, \quad (2)$$

with  $p \in \mathbb{R}$ . We found  $p = 1$  to be sufficient (thus using unscaled persistence values). Since Equation 2 results in a single scalar value for a persistence diagram, the summary statistics turn a sequence of time-varying persistence diagrams into a time series of scalar-valued summary statistics. Figure 2 depicts this for a single participant of our data.

**Qualitative evaluation.** Figure 3 shows an embedding obtained from our topological summary statistics (using multidimensional scaling based on the Euclidean distance between per-participant curves) compared to baseline embeddings, which we obtain from the two correlation matrices described in Section 3. We refer to them as BASELINE-TT (time-based) and BASELINE-PP (voxel-based; parcellated for computational ease), respectively (see Section A.4 for additional details). Both

<sup>4</sup>The term *total persistence* is sometimes used interchangeably for this norm.

topology-based embeddings are showing a split between participants. By colour-coding the age group of each participant, we see that topology-based embeddings separate adults (red) from children (other colours). The baselines, by contrast, do not exhibit such a clear-cut distinction.

**Quantitative evaluation.** To *quantify* the benefits of our proposed topological feature extraction pipeline, we set up a task in which we predict the age of the non-adult participants. Using a ridge regression and leave-one-out cross-validation (see Section A.5 for additional experimental details), we train models on either the curves of summary statistics (not the embeddings) or the baseline matrices, reporting the correlation coefficient in the table in Figure 3. Higher values indicate that the model is better suitable to predict the age. The SRM result comes from previous work on the same data set [58]; we note that our task is slightly different<sup>5</sup>. Overall, we observe strong correlations, indicating that topological features are highly useful for age prediction and carry salient information. Performance based on the occipital-temporal mask (OM) and on the XOR mask (XM) is higher than for the whole-brain mask (BM); we hypothesise that this partially due to the higher noise level of BM, whereas OM and XM focus only on a subset of the brain (which decreases the noise level). We also note that  $\|\mathcal{D}\|_\infty$ , which only considers the most persistence topological feature of a persistence diagram, performs best in the prediction task, possibly because it is more robust to small-scale noise

## 5.2 Dynamic analysis based on brain state trajectories

So far, we dealt only with overall summary statistics. Our framework also enables analysing the brain state of participants over time. We sidestep the aforementioned issue of persistence diagram metric computations by calculating *persistence images* [1] from the persistence diagrams. A persistence image is a function  $\Psi: \mathbb{R}^2 \rightarrow \mathbb{R}$  that turns a diagram  $\mathcal{D}$  into a surface via  $\Psi(z) := \sum_{x,y \in \mathcal{D}} w(x,y) \Phi(x,y,z)$ , where  $w(\cdot)$  is a fixed piecewise linear weight function and  $\Phi(\cdot)$  denotes a probability distribution, which is typically chosen to be a normalised symmetric Gaussian. By discretising  $\Psi$  (using an  $r \times r$  grid), a persistence diagram is transformed into an image<sup>6</sup>; this is depicted in Figure 1e. The main advantage of  $\Psi$  lies in embedding persistence diagrams into a space that is amenable to standard machine learning tools; moreover,  $\Psi$  affords defining and calculating *unique* means, as opposed to persistence diagrams [35, 36, 53]. Subsequently, we use  $r = 20$  and a Gaussian kernel with  $\sigma = 1.0$ ;  $\Psi$  is known to be impervious to such choices [1].

### 5.2.1 Cohort brain state trajectories

By evaluating  $\Psi(\mathcal{D}_2^{(i,j)})$  for each time step  $t_j$ , we turn the sequence of persistence diagrams of the  $i$ th participant into a matrix  $\mathbf{X}^{(i)} \in \mathbb{R}^{m \times r^2}$ , where the  $j$ th row corresponds to the ‘unravalled’ persistence image of time step  $t_j$ . We now calculate the sample mean  $\bar{\mathbf{X}}_k$  of each participant cohort, resulting in six matrices whose rows represent the average topological activity of participants in the respective cohort. Taking the Euclidean distance between persistence images as a proxy for their actual topological dissimilarity [1, Theorem 3], we calculate pairwise distances between rows of each  $\bar{\mathbf{X}}_k$  and embed them using PHATE [32], a powerful embedding algorithm for time-varying data. This turns  $\bar{\mathbf{X}}_k$  into a 2D *brain state trajectory* (where the state is measured using topological features). Figure 4 depicts the resulting trajectories for different masks. All brain state trajectories exhibit visually distinct behaviour in older and younger subjects. The youngest subjects are characterised by a simple ‘linear’ trajectory in the whole-brain mask, indicating that their processing of the movie is more sensory-driven. This pattern is visible in Figure 4b for young children in general: until 7.5 yr, sensory processing, analysed using the occipital-temporal mask, is comparatively simple. In older subjects, we observe more complex trajectories with higher entropy generally. Developmental differences are best indicated in Figure 4c, where we see that the overall trajectory shape becomes ‘adult-like’ *earlier* (and thus more complex). Since this mask is composed of more cognitive brain regions (rather than sensory ones), we hypothesise that this could indicate that older participants—including older children—are capable of connecting different aspects of the movie to their memories, for example, whereas the simpler trajectories of the two youngest cohorts in *all* brain masks may indicate that these participants are not comprehending the movie on a non-superficial level.

<sup>5</sup>Yates et al. [58] learn a shared set of features in adult participants to predict the age of non-adults.

<sup>6</sup>Intuitively, this can also be seen as a form of kernel density estimation on persistence diagrams.

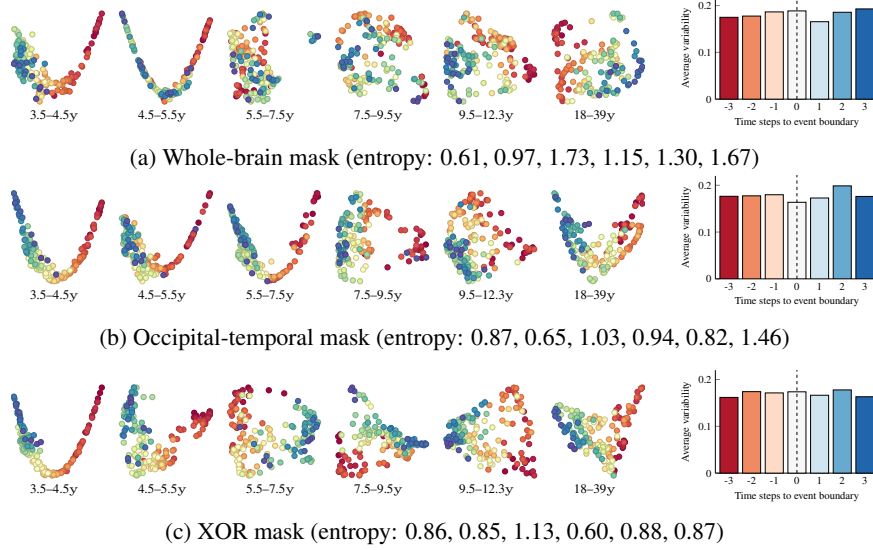


Figure 4: Cohort brain state trajectories for different masks. Annotations provide the age range of subjects in one cohort. Variability histograms are shown as the rightmost plot; their  $x$ -axis shows the time steps prior (negative) or after (positive) an event boundary, while their  $y$ -axis depicts across-cohort variability (please refer to Section 5.2.2 for more details);

## 5.2.2 Variability analysis

To quantify the variability across cohorts, we calculate the per-column maximum of each  $\bar{\mathbf{X}}_k$ , referring to the respective set of values as  $\|\bar{\mathbf{X}}_k\|_\infty \in \mathbb{R}^m$ ; the calculated values are the *equivalent* of the infinity norm evaluated (per time step) on a mean persistence image of the cohort. We finally calculate  $s = (\|\bar{\mathbf{X}}_1\|_\infty, \dots, \|\bar{\mathbf{X}}_6\|_\infty)$ , i.e. the sample standard deviation per time point, thus obtaining a *variability curve* of  $m$  time steps (see Figure A.5). To use this variability curve, we ran an online study to discover which salient events are detected by participants in the movie. Using 22 test subjects (with no overlap to the ones used in the fMRI data acquisition process), we followed Ben-Yakov and Henson [8] and determined consensus boundaries of events in the movie. We declare an event boundary to be *salient* if at least 7 participants agree, resulting in 20 events. Given this information, we collect the average variability over all events for a window of  $w = 3$  time steps before and after an event, leading to averaged variabilities  $\{s_1, \dots, s_7\}$ , where  $s_4$  corresponds to average variability at the event boundary itself (see histograms in Figure 4). It is our hypothesis that post-event and pre-event variability are different—in other words, our topological features capture cognitive differences across cohorts and events. To quantify this, we calculate  $s_{\text{pre}} := \max_{i \leq 3} s_i - \min_{i \leq 3} s_i$  and  $s_{\text{post}} := \max_{i \geq 5} s_i - \min_{i \geq 5} s_i$ . We set  $\theta := s_{\text{pre}} - s_{\text{post}}$  as our test statistic and perform a bootstrap procedure by sampling 20 time points at random and repeating the same calculation, thereby obtaining an empirical null distribution. This results in bootstrap samples  $\hat{\theta}_1, \dots, \hat{\theta}_{1000}$  serving as a null distribution  $\hat{\theta}$ , from which we obtain the achieved significance level (ASL) as  $\Pr(\hat{\theta} \geq \theta)$ .

The ASL values are 0.084 (whole-brain mask, BM), 0.045 (occipital-temporal mask, OM), and 0.396 (XOR mask, XM), respectively, indicating that the effect of capturing events is *strongest* in OM (and significant at the  $\alpha = 0.05$  level). This aligns well with the gradual differences between cohorts expressed in Figure 4b. Event differences are less pronounced in BM (which, as Figure 4a shows, is capturing more complex cohort patterns). Finally, event differences are *absent* in XM, showing that across-cohort variability is not consistent with event boundaries here, hinting at the fact that this mask might better be used to assess within-cohort variability rather than across-cohort variability. Please refer to Section A.7 for additional visualisations.

## 6 Conclusion

This paper demonstrates the potential of an unsupervised, non-parametric topology-based feature extraction framework for fMRI data, permitting both static and dynamic analyses. We showed that topological summary statistics are useful in an age prediction task. Using vectorised topological features descriptors, we also developed cohort brain state trajectories that show the time-varying behaviour of a cohort of participants (binned by age). Next, to highlight qualitative age-related differences in the overall cognition of participants, we were also able to uncover quantitative differences in event processing. In the future, we want to further analyse the *geometry* of brain state trajectories and link states back to events; a preliminary analysis (see [Section A.8](#)) finds significant differences between the mean curvature [19] of adult and non-adult participants, thus showcasing the explanatory potential of topological features.

### Broader impact

The primary contribution of this work—a novel, parameter-free way of extracting informative features from fMRI data—is of a computational nature. In general, we fully acknowledge that any researcher dealing with fMRI data analysis (not necessarily restricted to machine learning methods) has a big responsibility. Since our work is purely computational, we do not believe that it will have adverse ethical consequences, provided the experimental design is unbiased. For the same reason, our work is not specifically favouring or disfavouring any groups.

Beyond the immediate applications for fMRI data analysis, our work also has a broader applicability for the analysis of time-varying or structured neuroscience data in general. This includes other non-invasive techniques such as EEG or MEG, but also neuronal spike data from cell populations. Our work is appealing for such data because it does not *require* auxiliary representations such as graphs. We are thus convinced that the introduction of our directly-computable topological features will overall have beneficial outcomes.

As long-term goal, for example, our work could serve as a foundation to investigate neurological pathologies (such as depressive disorders) from a new, topological perspective. In general, our dynamic analyses also allow us to capture not just stable traits in different populations, but also the different mental states participants progress through while undergoing fMRI. As a generic feature descriptor of brain states, we would welcome a future in which topological features aid in understanding such traits or states.

### References

- [1] H. Adams, T. Emerson, M. Kirby, R. Neville, C. Peterson, P. Shipman, S. Chepushtanova, E. Hanson, F. Motta, and L. Ziegelmeier. Persistence images: A stable vector representation of persistent homology. *Journal of Machine Learning Research*, 18(8):1–35, 2017.
- [2] M. Allili, K. Mischaikow, and A. Tannenbaum. Cubical homology and the topological classification of 2D and 3D imagery. In *Proceedings of the IEEE International Conference on Image Processing*, volume 2, pages 173–176, 2001.
- [3] K. L. Anderson, J. S. Anderson, S. Palande, and B. Wang. Topological data analysis of functional MRI connectivity in time and space domains. In *Connectomics in NeuroImaging*, 2018.
- [4] C. Baldassano, J. Chen, A. Zadbood, J. W. Pillow, U. Hasson, and K. A. Norman. Discovering event structure in continuous narrative perception and memory. *Neuron*, 95(3):709–721.e5, 2017.
- [5] U. Bauer, M. Kerber, and J. Reininghaus. Distributed computation of persistent homology. In *Proceedings of the Meeting on Algorithm Engineering and Experiments (ALENEX)*, pages 31–38, 2014.
- [6] U. Bauer, M. Kerber, J. Reininghaus, and H. Wagner. PHAT – Persistent Homology Algorithms Toolbox. In H. Hong and C. Yap, editors, *Mathematical Software – ICMS 2014*, pages 137–143. Springer, 2014.
- [7] P.-L. Bazin and D. L. Pham. Topology-preserving tissue classification of magnetic resonance brain images. *IEEE Transactions on Medical Imaging*, 26(4):487–496, 2007.
- [8] A. Ben-Yakov and R. N. Henson. The hippocampal film editor: Sensitivity and specificity to event boundaries in continuous experience. *Journal of Neuroscience*, 38(47):10057–10068, 2018.

- [9] P. Bendich, J. S. Marron, E. Miller, A. Pieloch, and S. Skwerer. Persistent homology analysis of brain artery trees. *Annals of Applied Statistics*, 10(1):198–218, 2016.
- [10] L. Buitinck, G. Louppe, M. Blondel, F. Pedregosa, A. Mueller, O. Grisel, V. Niculae, P. Prettenhofer, A. Gramfort, J. Grobler, R. Layton, J. VanderPlas, A. Joly, B. Holt, and G. Varoquaux. API design for machine learning software: experiences from the `scikit-learn` project. In *ECML PKDD Workshop: Languages for Data Mining and Machine Learning*, pages 108–122, 2013.
- [11] M. Carrière, F. Chazal, Y. Ike, T. Lacombe, M. Royer, and Y. Umeda. PersLay: A neural network layer for persistence diagrams and new graph topological signatures. *arXiv e-prints*, art. arXiv:1904.09378, 2019.
- [12] C. Chen and H. Edelsbrunner. Diffusion runs low on persistence fast. In *Proceedings of the IEEE International Conference on Computer Vision*, pages 423–430, 2011.
- [13] P.-H. Chen, J. Chen, Y. Yeshurun, U. Hasson, J. Haxby, and P. J. Ramadge. A reduced-dimension fMRI shared response model. In C. Cortes, N. D. Lawrence, D. D. Lee, M. Sugiyama, and R. Garnett, editors, *Advances in Neural Information Processing Systems 28*, pages 460–468. Curran Associates, Inc., 2015.
- [14] D. Cohen-Steiner, H. Edelsbrunner, and D. Morozov. Vines and vineyards by updating persistence in linear time. In *Proceedings of the 22nd Annual Symposium on Computational Geometry*, pages 119–126, 2006.
- [15] D. Cohen-Steiner, H. Edelsbrunner, and J. Harer. Stability of persistence diagrams. *Discrete & Computational Geometry*, 37(1):103–120, 2007.
- [16] D. Cohen-Steiner, H. Edelsbrunner, and J. Harer. Extending persistence using Poincaré and Lefschetz duality. *Foundations of Computational Mathematics*, 9(1):79–103, 2009.
- [17] D. Cohen-Steiner, H. Edelsbrunner, J. Harer, and Y. Mileyko. Lipschitz functions have  $L_p$ -stable persistence. *Foundations of Computational Mathematics*, 10(2):127–139, 2010.
- [18] P. Dlotko and T. Wanner. Rigorous cubical approximation and persistent homology of continuous functions. *Computers & Mathematics with Applications*, 75(5):1648–1666, 2018.
- [19] M. P. do Carmo. *Differential Geometry of Curves and Surfaces*. Prentice-Hall, Inc., 1976.
- [20] H. Edelsbrunner and J. Harer. *Computational topology: An introduction*. American Mathematical Society, 2010.
- [21] H. Edelsbrunner, D. Letscher, and A. J. Zomorodian. Topological persistence and simplification. *Discrete & Computational Geometry*, 28(4):511–533, 2002.
- [22] C. T. Ellis, M. Lesnick, G. Henselman-Petrusek, B. Keller, and J. D. Cohen. Feasibility of topological data analysis for event-related fMRI. *Network Neuroscience*, 3(3):695–706, 2019.
- [23] O. Esteban, C. J. Markiewicz, R. W. Blair, C. A. Moodie, A. I. Isik, A. Erramuzpe, J. D. Kent, M. Goncalves, E. DuPre, M. Snyder, H. Oya, S. S. Ghosh, J. Wright, J. Durnez, R. A. Poldrack, and K. J. Gorgolewski. fMRIPrep: a robust preprocessing pipeline for functional MRI. *Nature Methods*, 16(1):111–116, 2019.
- [24] C. Giusti, R. Ghrist, and D. S. Bassett. Two’s company, three (or more) is a simplex. *Journal of Computational Neuroscience*, 41(1):1–14, 2016.
- [25] C. Hofer, R. Kwitt, M. Niethammer, and A. Uhl. Deep learning with topological signatures. In I. Guyon, U. V. Luxburg, S. Bengio, H. Wallach, R. Fergus, S. Vishwanathan, and R. Garnett, editors, *Advances in Neural Information Processing Systems 30*, pages 1634–1644. Curran Associates, Inc., 2017.
- [26] C. Hofer, R. Kwitt, M. Niethammer, and M. Dixit. Connectivity-optimized representation learning via persistent homology. In K. Chaudhuri and R. Salakhutdinov, editors, *Proceedings of the 36th International Conference on Machine Learning (ICML)*, number 97 in Proceedings of Machine Learning Research, pages 2751–2760. PMLR, 2019.
- [27] X. Hu, F. Li, D. Samaras, and C. Chen. Topology-preserving deep image segmentation. In H. Wallach, H. Larochelle, A. Beygelzimer, F. d’Alché-Buc, E. Fox, and R. Garnett, editors, *Advances in Neural Information Processing Systems 32*, pages 5657–5668. Curran Associates, Inc., 2019.
- [28] V. Khruikov and I. Oseledets. Geometry score: A method for comparing generative adversarial networks. In J. Dy and A. Krause, editors, *Proceedings of the 35th International Conference on Machine Learning (ICML)*, number 80 in Proceedings of Machine Learning Research, pages 2621–2629. PMLR, 2018.

- [29] S. Kumar, C. T. Ellis, T. O’Connell, M. M. Chun, and N. B. Turk-Browne. Searching through functional space reveals distributed visual, auditory, and semantic coding in the human brain. *bioRxiv*, 2020. doi: 10.1101/2020.04.20.052175.
- [30] R. Kwitt, S. Huber, M. Niethammer, W. Lin, and U. Bauer. Statistical topological data analysis — a kernel perspective. In C. Cortes, N. D. Lawrence, D. D. Lee, M. Sugiyama, and R. Garnett, editors, *Advances in Neural Information Processing Systems 28*, pages 3070–3078. Curran Associates, Inc., 2015.
- [31] N. Milosavljević, D. Morozov, and P. Skraba. Zigzag persistent homology in matrix multiplication time. In *Proceedings of the 27th Annual Symposium on Computational Geometry*, pages 216–225, 2011.
- [32] K. R. Moon, D. van Dijk, Z. Wang, S. Gigante, D. B. Burkhardt, W. S. Chen, K. Yim, A. v. d. Elzen, M. J. Hirn, R. R. Coifman, N. B. Ivanova, G. Wolf, and S. Krishnaswamy. Visualizing structure and transitions in high-dimensional biological data. *Nature Biotechnology*, 37(12):1482–1492, 2019.
- [33] M. Moor, M. Horn, B. Rieck, and K. Borgwardt. Topological autoencoders. *arXiv e-prints*, art. arXiv:1906.00722, 2019.
- [34] M. Mrozek and T. Wanner. Coreduction homology algorithm for inclusions and persistent homology. *Computers & Mathematics with Applications*, 60(10):2812–2833, 2010.
- [35] E. Munch. *Applications of Persistent Homology to Time Varying Systems*. PhD thesis, Duke University, 2013.
- [36] E. Munch, K. Turner, P. Bendich, S. Mukherjee, J. Mattingly, and J. Harer. Probabilistic Fréchet means for time varying persistence diagrams. *Electronic Journal of Statistics*, 9(1):1173–1204, 2015.
- [37] V. Nanda. *Discrete Morse Theory For Filtrations*. PhD thesis, Rutgers University, 2012.
- [38] K. N. Ramamurthy, K. Varshney, and K. Mody. Topological data analysis of decision boundaries with application to model selection. In K. Chaudhuri and R. Salakhutdinov, editors, *Proceedings of the 36th International Conference on Machine Learning (ICML)*, number 97 in Proceedings of Machine Learning Research, pages 5351–5360. PMLR, 2019.
- [39] H. Richardson, G. Lisandrelli, A. Riobueno-Naylor, and R. Saxe. Development of the social brain from age three to twelve years. *Nature Communications*, 9(1):1–12, 2018.
- [40] B. Rieck, C. Bock, and K. Borgwardt. A persistent Weisfeiler–Lehman procedure for graph classification. In K. Chaudhuri and R. Salakhutdinov, editors, *Proceedings of the 36th International Conference on Machine Learning*, volume 97 of *Proceedings of Machine Learning Research*, pages 5448–5458. PMLR, 2019.
- [41] B. Rieck, M. Togninalli, C. Bock, M. Moor, M. Horn, T. Gumbsch, and K. Borgwardt. Neural persistence: A complexity measure for deep neural networks using algebraic topology. In *International Conference on Learning Representations (ICLR)*, 2019.
- [42] J. B. T. M. Roerdink and A. Meijster. The watershed transform: Definitions, algorithms and parallelization strategies. *Fundamenta Informaticae*, 41:187–228, 2000.
- [43] M. Royer, F. Chazal, C. Levrard, Y. Ike, and Y. Umeda. ATOL: Measure vectorisation for automatic topologically-oriented learning. *arXiv e-prints*, art. arXiv:1909.13472, 2019.
- [44] M. Saggat, O. Sporns, J. Gonzalez-Castillo, P. A. Bandettini, G. Carlsson, G. Glover, and A. L. Reiss. Towards a new approach to reveal dynamical organization of the brain using topological data analysis. *Nature Communications*, 9(1):1399, 2018.
- [45] F. A. N. Santos, E. P. Raposo, M. D. Coutinho-Filho, M. Copelli, C. J. Stam, and L. Douw. Topological phase transitions in functional brain networks. *Physical Review E*, 100:032414, 2019.
- [46] N. Saul and C. Tralie. *Scikit-TDA: Topological data analysis for Python*, 2019. URL <https://doi.org/10.5281/zenodo.2533369>.
- [47] A. Schaefer, R. Kong, E. M. Gordon, T. O. Laumann, X.-N. Zuo, A. J. Holmes, S. B. Eickhoff, and B. T. T. Yeo. Local–global parcellation of the human cerebral cortex from intrinsic functional connectivity MRI. *Cerebral Cortex*, 28(9):3095–3114, 2017.
- [48] G. Singh, F. Méholi, and G. Carlsson. Topological methods for the analysis of high dimensional data sets and 3D object recognition. In *Eurographics Symposium on Point-Based Graphics*, 2007.

- [49] A. E. Sizemore, J. E. Phillips-Cremins, R. Ghrist, and D. S. Bassett. The importance of the whole: Topological data analysis for the network neuroscientist. *Network Neuroscience*, 3(3):656–673, 2019.
- [50] P. Sohn and K. Reher. Partly Cloudy [motion picture], 2009. Pixar Animation Studios and Walt Disney Pictures.
- [51] D. Strömbom. Persistent homology in the cubical setting: Theory, implementations and applications. Master’s thesis, Luleå University of Technology, 2007.
- [52] N. B. Turk-Browne. Functional interactions as big data in the human brain. *Science*, 342(6158):580–584, 2013.
- [53] K. Turner, Y. Mileyko, S. Mukherjee, and J. Harer. Fréchet means for distributions of persistence diagrams. *Discrete & Computational Geometry*, 52(1):44–70, 2014.
- [54] K. Vodrahalli, P.-H. Chen, Y. Liang, C. Baldassano, J. Chen, E. Yong, C. Honey, U. Hasson, P. Ramadge, K. A. Norman, and S. Arora. Mapping between fMRI responses to movies and their natural language annotations. *NeuroImage*, 180:223–231, 2018.
- [55] H. Wagner, C. Chen, and E. Vučini. Efficient computation of persistent homology for cubical data. In R. Peikert, H. Hauser, H. Carr, and R. Fuchs, editors, *Topological Methods in Data Analysis and Visualization II: Theory, Algorithms, and Applications*, pages 91–106. Springer, 2012.
- [56] B. Wang and G.-W. Wei. Object-oriented persistent homology. *Journal of Computational Physics*, 305: 276–299, 2016.
- [57] Y. Wang, J. D. Cohen, K. Li, and N. B. Turk-Browne. Full correlation matrix analysis (FCMA): An unbiased method for task-related functional connectivity. *Journal of Neuroscience Methods*, 251:108–119, 2015.
- [58] T. S. Yates, C. T. Ellis, and N. B. Turk-Browne. Emergence and organization of adult brain function throughout child development. *bioRxiv*, 2020. doi: 10.1101/2020.05.09.085860.
- [59] Q. Zhao and Y. Wang. Learning metrics for persistence-based summaries and applications for graph classification. In H. Wallach, H. Larochelle, A. Beygelzimer, F. d’Alché-Buc, E. Fox, and R. Garnett, editors, *Advances in Neural Information Processing Systems 32*, pages 9855–9866. Curran Associates, Inc., 2019.

## A Appendix

The following sections provide additional details about the experiments as well as a brief glimpse into other analyses that we are actively pursuing for future work.

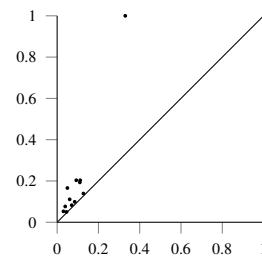
### A.1 An intuitive introduction to persistent homology

Persistent homology was developed as a ‘shape descriptor’ for real-world data sets, where the idealised notions of algebraic topology do not necessarily apply any more. This is illustrated by the subsequent figure, which deals with a point cloud that has a roughly circular shape. Notice that this shape is immediately recognisable to humans, but from the perspective of algebraic topology, it is merely a collection of points with a trivial shape.



We observe that we *can* analyse this point cloud by picking an appropriate scale parameter. More precisely, if we start connecting points that are within a certain distance  $\epsilon$  to each other, we obtain a nested sequence of simplicial complexes (in our context, this term is synonymous with a graph) as we increase  $\epsilon$ . This is a special type of filtration—a filtration based on pairwise distances, and the resulting simplicial complexes are depicted above. It is now possible to calculate Betti numbers for each of these complexes. Since we are only dealing with 2D points, there are only two relevant Betti numbers, namely  $\beta_0$  and  $\beta_1$ , corresponding to the number of connected components and the number of cycles, respectively. Suppose now that we *track* these numbers for each one of the steps in the filtration; moreover, suppose we have a way of making the individual steps in the filtration as small as possible such that we never miss any changes in  $\beta_0$  and  $\beta_1$ . For every topological feature—every component and every cycle—we can thus measure precisely when a feature was created and when it was destroyed.

**Persistence diagram.** This information is collected in the persistence diagram, which summarises all topological activity. In this example, the persistence diagram of the 1-dimensional topological features contains a few points, each one of them corresponding to one specific cycle in the data. The axes correspond to the scale parameter (their actual values can be safely ignored for this illustrative example). The  $x$ -axis shows the threshold at which a cycle was *created*, i.e. at which there is a ‘hole’ in the corresponding simplicial complex, while the  $y$ -axis depicts the threshold at which this hole is *destroyed*, i.e. closed. We do not specifically indicate this here, but cycles are destroyed whenever all points that are involved in their creation are connected to each other. Put differently, this means that we ignore cycles created by individual triangles of points, for example, as they are qualitatively different from cycles created by arranging points in such a circular shape (there are more technical reasons for this restriction). In any case, the persistence diagram demonstrates that virtually all cycles—depicted as points—occur at small scales, except for *one*. This coincides with our intuition: we do not perceive such a point cloud to have a lot of large-scale cycles. The persistence diagram thus serves as an intuitive feature descriptor: points that occur at large scales are far removed from the diagonal (and have a high persistence), whereas the small-scale features cluster around the diagonal.

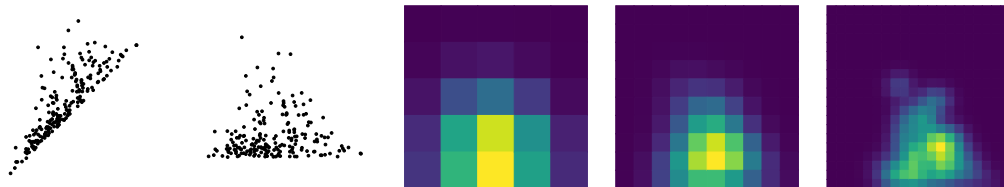


A persistence diagram of the 1-dimensional topological features (cycles).

The interesting fact is that knowing the persistence diagram also makes it possible for us to ‘guess’ the number of relevant scales of a point cloud! In this example, we would possibly state that there is only *one* useful scale at which to analyse the data, namely the scale for which the cycle structure becomes topologically apparent. In general, this will differ based on the data set. Persistent homology does not force us to prefer a scale, making it suitable for the analysis of real-world data sets. The ingenious realisation of Edelsbrunner et al. [21] was that there is no reason to ‘guess’ scales or compute Betti

numbers per step, as we described it above. Instead, it is possible to obtain information about *all* potential scales by a single pass through the data, making this a highly-efficient algorithm (at least as long as the dimension of the input data is bounded; calculating topological features for dimensions  $d \gg 3$  efficiently is still a topic of ongoing research).

**Persistence images.** Since the metric structure of persistence diagrams is known to be complex [36], various kernel-based and ‘vectorisation’ methods exist. In the main text, we focus on *persistence images* [1], a technique that essentially estimates the density of a persistence diagram and uses a grid to obtain a fixed-size representation. Such representations may then be used for downstream processing tasks. As a worked example, consider the following persistence diagram. After rotating it so that the diagonal becomes the new  $x$ -axis, we can perform density estimates with different resolutions. The density estimator, which is by default a Gaussian kernel, can be adjusted as well, but Adams et al. [1] mention that this does *not* have a large influence on the results (whereas the resolution should be sufficiently large to capture differences). In the main paper, we use a smoothing value of  $\sigma = 1$  and a resolution of  $r = 20$ , resulting in 400-dimensional vectors. We also calculated different resolutions and smoothing values, but the results are virtually identical, unless the resolution is decreased too much: recall that a single persistence diagram of one participant has around 10000 features; reducing them to a, say,  $5 \times 5$  image results in a large loss of information.



## A.2 Properties of cubical complexes

Figure A.3 depicts the differences between cubical complexes and simplicial complexes. The cubical complex is ‘aligned’ with a regular grid and does *not* force us to choose between an interpolation scheme. For a simplicial complex, however, the calculation of topological features in dimensions 1 and 2 necessitates the creation of 2-simplices, i.e. triangles. This, in turn, requires us to ‘pick’ between two triangulation schemes that result in different connectivities between the original vertices. In the worst case, this could lead to subtle differences in filtrations, since the new edges need to be weighted accordingly.

## A.3 fMRI pre-processing

The fMRI data acquisition used the following parameters: gradient-echo EPI sequence: TR = 2 s, TE = 30 ms, flip angle =  $90^\circ$ , matrix =  $64 \times 64$ , slices = 32, interleaved slice acquisition. Data were collected using the standard Siemens 32-channel head coil for adults and older children. One of two custom 32-channel phased-array head coils was used for younger children (smallest coil: N = 3; M = 3.91, SD = 0.42 years old; smaller coil: N = 28; M = 4.07, SD = 0.42, years old). Acquisition parameters differed slightly across participants but all fMRI data were re-sampled to have the same voxel size: 3 mm isotropic with 10% slice gap. A T1-weighted structural image was also collected for all subjects (MPRAGE sequence: GRAPPA = 3, slices = 176, resolution = 1 mm isotropic, adult coil FOV = 256 mm, child coils FOV = 192 mm). Imaging data were pre-processed using fMRIPrep v1.1.8 [23].

## A.4 Baselines

As additional comparison partners, we calculate a time point correlation matrix and a spatial correlation matrix (see Section 3). These matrices are calculated from the time-varying fMRI data of a single participant, which is a 4D tensor indexed by time steps and spatial coordinates. By ‘unravelling’ the spatial dimensions of the tensor (using a *row-major ordering*, for example), the 4D tensor becomes a 2D tensor, i.e. a matrix in which each row corresponds to a single time step, and the columns correspond to voxels in the aforementioned order. From this  $m \times N$  matrix, where  $m$  denotes the

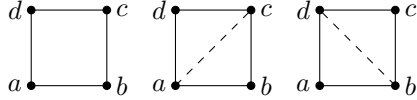


Figure A.3: If we use a cubical complex (left; only a single square cell is shown) we do not have to choose an interpolation scheme for voxel-based data. Function values can be stored in the vertices ( $a$ ,  $b$ ,  $c$ ,  $d$ ) and interpolation happens along the edges. For simplicial complexes, however, we need to convert the square into a triangle (the same issue occurs in higher dimensions with cubes and tetrahedra, respectively). This conversion to triangles leaves us with two ways of interpolating that will typically lead to different results. In one case, we are interpolating between  $a$  and  $c$ , in the other case between  $b$  and  $d$ . Neither one of these edges exist in the original data, though.

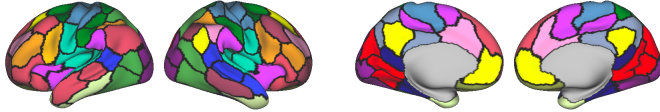


Figure A.4: A schematic illustration of the parcels used to make the computation of a full correlation matrix computationally feasible. This only pertains to the BASELINE-PP method.

number of time steps as in the main paper and  $N$  denotes the total number of voxels, we can calculate Pearson product-moment correlation coefficients. If we do this for the original matrix, we obtain an  $m \times m$  *time point correlation matrix*, which we denote by BASELINE-TT (i.e. a time-by-time matrix).

Conversely, we can transpose the matrix to obtain a voxel-by-voxel correlation matrix—referred to as a *full correlation matrix* (FCMA). This matrix has dimensions  $N \times N$ , though, which is computationally prohibitive for most applications. As a more feasible calculation, we calculate the spatial correlation matrix from a parcellated data set. We use 100 parcels from 17 functional networks Schaefer et al. [47], depicted in Figure A.4, so that we obtain a  $100 \times 100$  correlation matrix, which we refer to as BASELINE-PP to indicate that parcellated data was used to obtain this matrix.

### A.5 Age prediction experimental details

For the age prediction experiment from Section 5.1, we use a standard ridge regression classifier with internal leave-one-out cross-validation [10] for its regularisation strength parameter  $C \in \{0.1, 1.0, 10.0\}$ . Internally, the classifier optimises the  $R^2$  score, i.e. the coefficient of determination. We report the correlation coefficient in the table in order to be aligned with the reporting in previous publications, though. We standardise *all* features prior to using them for the classifier. The classifier is then used in a leave-one-out cross-validation scheme.

Since the input features have different cardinalities (the parcellated voxel-by-voxel matrix, for example, has a cardinality of  $100^2$ , which will lead to severe overfitting, we reduce the baseline matrices to 100 dimensions using principal component analysis. Moreover, to demonstrate the impact

Table A.1: Additional experimental results for the age prediction tasks. In contrast to the table in the main paper, here we show both the correlation coefficient (CC; higher values are preferable) and the mean squared error (MSE; lower values are preferable) whenever available.

Method	BM		OM		XM	
	CC	MSE	CC	MSE	CC	MSE
BASELINE-TT	0.09	10.15	0.02	13.81	0.24	7.19
BASELINE-PP	0.41	6.23	0.40	6.40	0.40	6.65
SRM	0.44	6.05	—	—	—	—
$\ \mathcal{D}\ _1$	0.46	4.27	0.67	2.95	0.48	4.17
$\ \mathcal{D}\ _\infty$	<b>0.61</b>	<b>3.38</b>	<b>0.77</b>	<b>2.20</b>	<b>0.73</b>	<b>2.53</b>

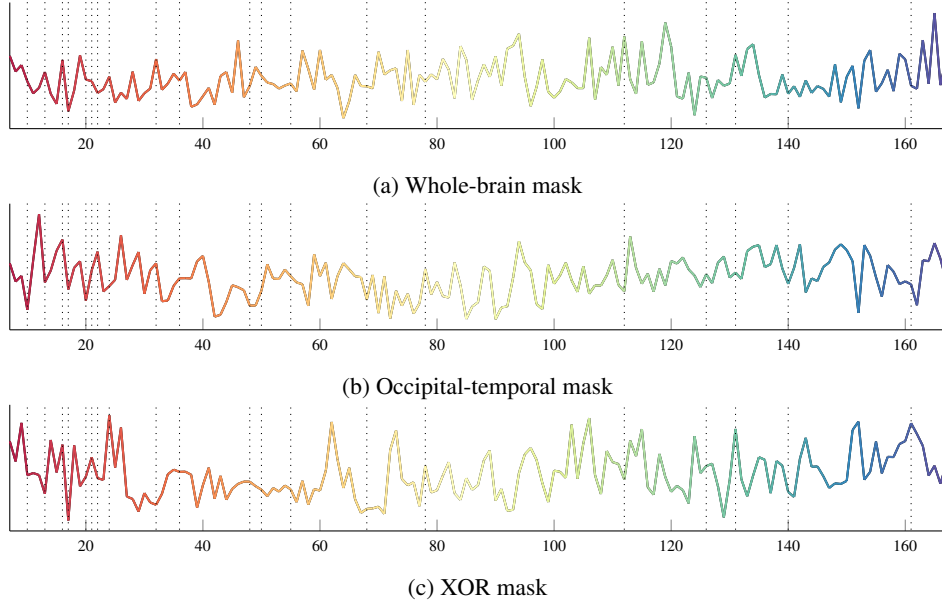


Figure A.5: Across-cohort variability curves for the different masks. The dotted lines represent the events. Generally, events are aligned with local extrema of the curves.

of our topological summary statistics, we only use summary statistics from the second half of the time series, resulting in *less* than 100 features. We observe that the results are highly stable; even reducing the number of selected features to less than 10 has no noticeable effect on the resulting regression model, indicating the informativeness of topology for this task.

Table A.1 shows extended results for this experiment, including MSE values (another goodness-of-fit measure) that were excluded from the table in the main paper because of the incomparability to existing methods. To reproduce the values in this table, please use the provided `predict_age.py` script.

### A.6 Proof of the stability theorem

*Proof.* Let  $\mathcal{V} := [0, 1]^3$ ; this is not a restriction because fMRI volumes are bounded, so they are always homeomorphic to this ‘standard cube’. Hence,  $\mathcal{V}$  is a compact metric space that can be triangulated. Since  $f$  and  $g$  are continuous functions (at least this is the ‘idealised’ view in which we have access to an infinite number of samples, the stability follows from the main theorem of Cohen-Steiner et al. [15]. ■

### A.7 Across-cohort variability analysis

For the across-cohort variability analysis, Figure A.5 shows the ‘raw’ curves for each of the masks, annotated with the respective events. As described in Section 5.2.2, we *pool* variability for all events and analyse the resulting histograms. This construction loses some information, but is a simple way to assess overall differences in variability.

### A.8 Curvature analysis

The curvature  $\kappa$  of a differentiable curve measures how sharply the trajectory curves at a given point *on* the curve. A circle, for example, always has curvature of 1 at each point, while a straight line, by contrast, always has a curvature of 0. We hypothesise that the curvature of brain state trajectories can help to further characterise subjects by looking at topological activity from a geometric point of view.

Let  $x(t)$  be the  $x$ -coordinate of a brain trajectory (as shown in Figure 4) at time  $t$  and  $y(t)$  its respective  $y$ -coordinate. Furthermore, let us define  $\dot{x}$  as the first derivative of  $x$  with respect to  $t$ ;

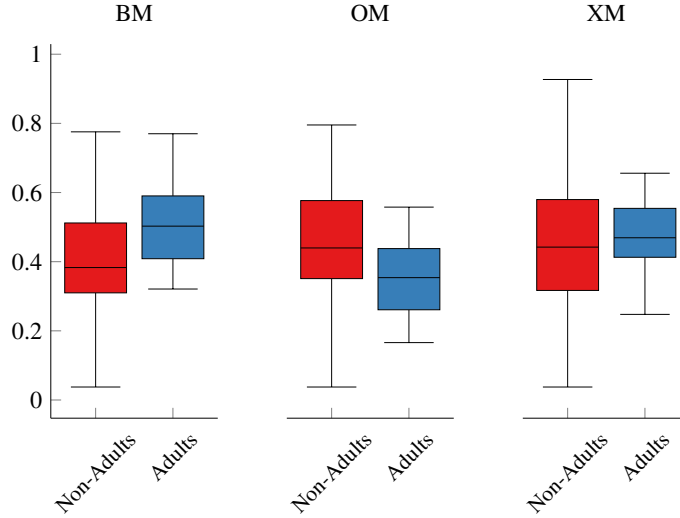


Figure A.6: Distribution of brain state trajectory curvature values at event boundaries. The distributions differ significantly for BM ( $p_{KS} = 0.00406$  and  $p_t = 0.0327$ ) and OM ( $p_{KS} = 0.0276$  and  $p_t = 0.0402$ ), but not so for XM ( $p_{KS} = 0.0861$  and  $p_t = 0.282$ ).

equivalently,  $\ddot{x}$  denotes the second derivative. Curvature can then be expressed as

$$\kappa = \frac{|\dot{x}\ddot{y} - \dot{y}\ddot{x}|}{(\dot{x}^2 + \dot{y}^2)^{\frac{3}{2}}} \quad (3)$$

Notice that curvature is an inherently *local* quantity. We computed  $\kappa$  for all brain state trajectories of all cohorts and for all three segmentation masks. We then investigated the differences in  $\kappa$  around event boundaries, similar to the variability analysis in Section 5.2.2. Figure A.6 shows the distribution of curvature values when stratifying the subjects into *adults* and *non-adults*. We find significant differences (at the  $\alpha = 0.05$  level) in the distribution of values in terms of a two-sided Kolmogorov–Smirnov test ( $p_{KS}$ ) and in terms of a  $T$ -test ( $p_t$ ) for both BM and OM, whereas the differences in XM are not considered to be significant.